



**HAL**  
open science

## **A hollow-core fiber based stand-alone multimodal (2-photon, 3-photon, SHG, THG) nonlinear flexible imaging endoscope system**

Dylan Septier, G. Brévalle-Wasilewski, Eloïse Lefebvre, N. Gajendra Kumar,  
Y. Wang, A. Kaszas, Hervé Rigneault, Alexandre Kudlinski

► **To cite this version:**

Dylan Septier, G. Brévalle-Wasilewski, Eloïse Lefebvre, N. Gajendra Kumar, Y. Wang, et al.. A hollow-core fiber based stand-alone multimodal (2-photon, 3-photon, SHG, THG) nonlinear flexible imaging endoscope system. IEEE Journal of Selected Topics in Quantum Electronics, In press, 10.1109/JSTQE.2024.3411821 . hal-04608983

**HAL Id: hal-04608983**

**<https://hal.science/hal-04608983>**

Submitted on 12 Jun 2024

**HAL** is a multi-disciplinary open access archive for the deposit and dissemination of scientific research documents, whether they are published or not. The documents may come from teaching and research institutions in France or abroad, or from public or private research centers.

L'archive ouverte pluridisciplinaire **HAL**, est destinée au dépôt et à la diffusion de documents scientifiques de niveau recherche, publiés ou non, émanant des établissements d'enseignement et de recherche français ou étrangers, des laboratoires publics ou privés.

# A hollow-core fiber based stand-alone multimodal (2-photon, 3-photon, SHG, THG) nonlinear flexible imaging endoscope system

D. Septier, G. Brévalle-Wasilewski, E. Lefebvre, N. Gajendra Kumar, Y. J. Wang, A. Kaszas, H. Rigneault, and A. Kudlinski

**Abstract**—Multimodal nonlinear endoscopes have been a topic of intense research over the past two decades, enabling sub-cellular and label-free imaging in areas not reachable with table-top microscopes. They are sophisticated systems that can be implemented on an optical table in a lab environment, but they cannot be easily moved within or out of the lab. We present here a multimodal and flexible nonlinear endoscope system able to perform two-photon excited fluorescence and second harmonic generation imaging with a stand-alone and movable compact integrating a compact ultrashort laser source. In addition, the system can perform three-photon excited fluorescence and third harmonic generation imaging thanks to a delivery optical fiber that connects a large frame laser system to the stand-alone kart. The endoscopic fiber probes and delivery optical fibers are based on functionalized negative curvature hollow core fibers. The endoscope distal head has a diameter  $<2.2$  mm and can perform nonlinear imaging at max 10 frames/s over a field of view up to  $600$   $\mu\text{m}$  with a  $\sim 1$   $\mu\text{m}$  spatial resolution.

**Index Terms**—Hollow core fibers, nonlinear micro-endoscopy, multiphoton endoscope, movable endoscope system

## I. INTRODUCTION

Manuscript received xxx; revised xxx; accepted xxx. Date of publication xxx; date of current version xxx.

D. Septier was with Univ. Lille, CNRS, UMR 8523 - PhLAM - Physique des Lasers Atomes et Molécules, Lille, France. He is now with Lightcore Technologies, Marseille, France. ([dylan.septier@lightcore.tech](mailto:dylan.septier@lightcore.tech))

G. Brévalle-Wasilewski is with Lightcore Technologies, Marseille, France. E. Lefebvre is with Univ. Lille, CNRS, UMR 8523 - PhLAM - Physique des Lasers Atomes et Molécules, Lille, France and with Lightcore Technologies, Marseille, France.

N. Gajendra was with Aix Marseille Univ, CNRS, Centrale Med, Institut Fresnel, Marseille, France. He is now with Lightcore Technologies, Marseille, France.

Y. J. Wang is with Lightcore Technologies, Marseille, France.

A. Kaszas is with Lightcore Technologies and the Multimodal Neurotechnology Group from the Institute of Cognitive Neuroscience and Psychology at the HUN-REN Research Centre for Natural Sciences (Hungary)

H. Rigneault is with Aix Marseille Univ, CNRS, Centrale Med, Institut Fresnel, Marseille, France. ([herve.rigneault@fresnel.fr](mailto:herve.rigneault@fresnel.fr))

A. Kudlinski is with Univ. Lille, CNRS, UMR 8523 - PhLAM - Physique des Lasers Atomes et Molécules, Lille, France. ([alexandre.kudlinski@univ-lille.fr](mailto:alexandre.kudlinski@univ-lille.fr))

The reported studies have been conducted following the EU ethical rules on animal. Mouse brain slices are coming from the Institut des Neurosciences de la Méditerranée following INMED agreement number B13-055-19 and OGM agreement number 5817. The fresh pig eyeball were graciously obtained from the euthanized pig (Département Hospitalo-Universitaire de Recherche et d'Enseignement - Dhure). *In vivo* imaging shown in Fig. 12 and Supp info movie 2, 3 and 4 were done with the consent of G. B.-W.

Color versions of one or more of the Figs in this article are available online at <http://ieeexplore.ieee.org>

MULTIPHOTON microscopy [1]–[3] has now matured and is widely recognized as an essential technology for applications in biological and medical sciences. The appeal of multiphoton microscopy lies in two key factors. Firstly, it offers a variety of nonlinear contrast mechanisms activated by short laser pulses with near-infrared wavelengths, enabling penetration into biological tissues [4]. Some contrast mechanisms, like two-photon excited fluorescence (2-photon) [5], require fluorescent molecules, while others, termed 'label-free' contrasts, can be activated without any labeling or staining. These include two-photon excited auto-fluorescence [6], second (SHG) [7] and third (THG) [8] harmonic generation, four-wave mixing (FWM) [9], such as chemical-sensitive coherent anti-Stokes Raman scattering (CARS) and stimulated Raman scattering (SRS) [10], [11] along with various pump-probe schemes [12] addressing transient absorption or vibrations lasting longer than the excitation pulse. Tremendous applications have been demonstrated in many fields of biology [13], [14] but also in medical sciences [15], [16]. Besides its successful implementation in microscopy [17], there have been numerous attempts to implement multiphoton imaging in flexible probes that can be handheld or inserted in constrained environments, such as those found in endoscopy for the exploration of the human body. We deliberately do not address in this paper the miniature-microscopes developed for neuroscience applications that have larger lateral dimensions and animal head-attachment requirements. Tubular multiphoton endoscopes have been reported using MEMS [18] or resonant piezo-tubes [19]–[21] to build tiny scanners that can be located at the endoscope distal head. Imaging fiber bundles have also been used to move the scanning procedure away from the sample side, this remove all moving parts or driving currents from the distal endoscope head [22]. The main challenge of multiphoton endoscope is to deliver ultra-short pulses at the sample plane to activate the nonlinear contrasts and several solutions have been reported such as pre-compensation schemes [23]–[25] or using hollow core fibers [26], [27]. With these advances multiple flexible multimodal nonlinear endoscopy has been reported using one or a combination of the 2-photon, SHG, THG and CARS contrast mechanisms [19], [26], [28]–[37] and a recent review can be found in [38]. So far three-photon excited fluorescence (3-photon) flexible endoscope reports are more sparse [29] and most of the current 3-photon implementation are using rigid graded index (GRIN) lenses [39], [40]. Most implementations of multiphoton flexible endoscopes are lab-

based systems that cannot be easily moved within the lab space or to an external field where measurements need to be performed. In this paper, we overcome this limitation and present a stand-alone integrated flexible multiphoton endoscope system placed on a movable kart platform. We provide a comprehensive presentation of its hardware and software parts to enable nonlinear imaging to non-experts. This complements our previous works that concentrated on the hollow core fiber itself and its functionalization [27], [29]. The nonlinear endoscope system includes a small frame femtosecond (fs) laser but can also be connected through a 'delivery fiber' to a larger frame multiphoton fs or picosecond (ps) laser platform to extend multiphoton contrasts. The system is controlled by dedicated user-friendly software and can perform 2-photon and SHG using in in-built laser as well as 3-photon and THG using the fiber delivery from a larger laser frame. The endoscope can perform imaging over field of view (FoV) up to 600  $\mu\text{m}$  with a resolution of  $\sim 1 \mu\text{m}$  at a maximum frame rate of 10 frames/s (fps).

## II. DOUBLE-CLAD HOLLOW CORE FIBER AND FUNCTIONALIZATION OF THE FIBER TIP

The nonlinear endoscope system developed is based on double clad hollow core negative curvature optical fibers similar to the ones presented in details in [27], [29]. They are indeed excellent candidates to deliver ultrashort pulses thanks to their intrinsic low group velocity dispersion (GVD) and non-linearity [41]–[43]. However, they need to be functionalized in order to strongly reduce the output spot size, which is required for high resolution imaging [26], [29]. We are addressing all these issues in this section.

### A. Double-clad anti-resonant hollow core fiber

The inset of Fig. 1(a) shows a scanning electron microscope (SEM) image of the fiber used to build the flexible endoscope, with a close-up on the hollow core region. The design is made of 7 non-touching capillaries of 14  $\mu\text{m}$  average external diameter, 8  $\mu\text{m}$  average separation and 350 nm average thickness. The core radius is 18  $\mu\text{m}$ . The silica cladding surrounding the central hollow region is able to guide light *via* total internal reflection thanks to a low-index polymer coating (not shown on the picture). The numerical aperture (NA) of the double clad was measured to be 0.38 at 450 nm [27]. Fig. 1(a) shows the attenuation spectrum obtained from a cutback measurement from 17 m to 1.5 m in the first antiresonant window. The attenuation is 0.32 dB/m at 920 nm and 0.31 dB/m at 1300 nm, which are the two wavelengths of main interest here. The fiber was found to be single mode for fiber samples longer than 2 m, due to the differential loss between the fundamental mode and higher-order modes for this particular fiber. The  $1/e^2$  mode field diameter (MFD) was measured to be equal to 24  $\mu\text{m}$  at 920 nm. Fig. 1(b) shows the measured and simulated GVD, respectively displayed with markers and solid line. The measurement was done using a low coherence Mach-Zehnder interferometer [44] and the simulation was performed with the analytical model [45] using the geometrical parameters listed above. The GVD value is 0.85 and 2.1 ps/nm/km at 920 and 1300 nm, respectively.

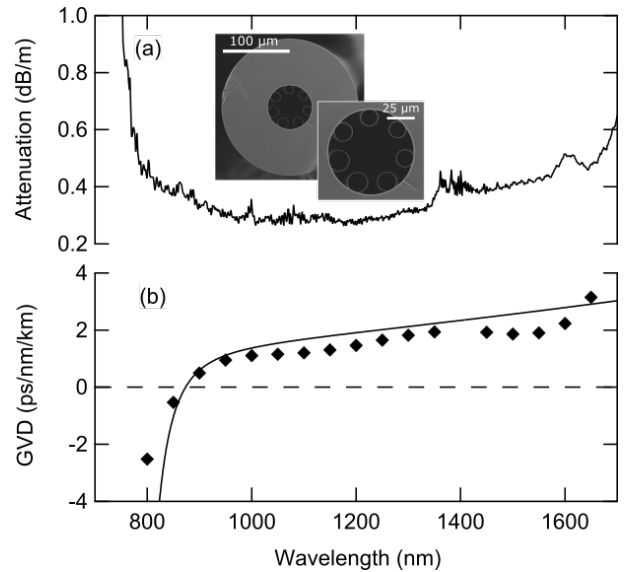


Fig. 1. Hollow core fiber: (a) Measured attenuation spectrum. Inset: SEM images. (b) Measured GVD (markers) and simulation (solid line) using the parameters in the text and the model from [45].

### B. Functionalization of the fiber tip

Since the MFD of the hollow core fiber is as large as 24  $\mu\text{m}$ , it needs to be strongly reduced for endoscopy application that require a  $\sim 1 \mu\text{m}$  spot size at the sample plane. Since bulky optics cannot be used in the endoscope distal head, this can be done for example by splicing silica beads [26], [27] or short pieces of graded-index (GRIN) fibers [29] at the output facet. We chose this last solution because in addition to focusing the output beam, it allows to seal the fiber end-face and brings more mechanical robustness than the bead splicing method. For a given GRIN fiber, the smallest focal spot is obtained when the fiber length is exactly half the self-imaging period [46]. In this case, the focal spot is located on the GRIN fiber end-surface. This is fine for the pulse duration around  $\sim 150$  fs and pulse energy in the  $\sim \text{nJ}$  range required for 2-photon absorption. However, 3-photon absorption requires significantly shorter pulses ( $< 100$  fs) with higher energy ( $\sim \mu\text{J}$ ), such that a parasitic THG signal can be generated at the interface between the GRIN fiber end-face and air [29]. In this case, the GRIN fiber can be shortened so that the focal spot is located further away in air, at the expense of a less efficient MFD reduction (*i.e.* focalization). This shortening reduces the energy density at the GRIN fiber/air interface and therefore strongly reduces the parasitic THG signal. In the present work, we present two different fiber probes: the first one (labeled 2-photon fiber) is optimized for 2-photon absorption and features a GRIN fiber length that performs the smallest MFD at the GRIN fiber/air surface and the second one (labeled 3-photon fiber) has a GRIN fiber length optimized for 3-photon absorption and performs a smaller MFD reduction but is free of THG noise.

Fig. 2(a) shows an optical microscope image of the 2-photon fiber that has a diameter of 200  $\mu\text{m}$ . The double-clad hollow core fiber is on the left and the GRIN fiber which has been spliced is located on the right. The GRIN fiber has a core

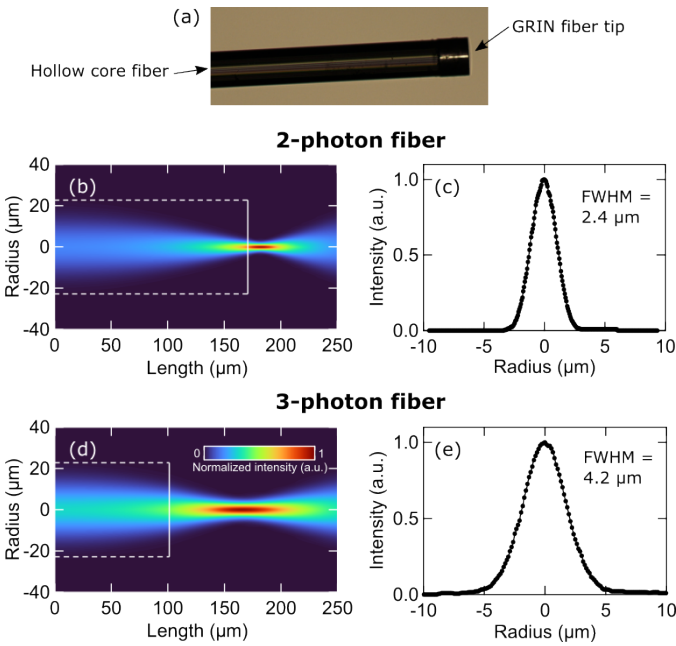


Fig. 2. (a) Optical microscope image of a hollow core fiber functionalized with a GRIN fiber. (b) Simulation of the optical intensity evolution at 920 nm for a GRIN fiber length of 171  $\mu\text{m}$ . White dashed lines represent the core/cladding interface of the GRIN fiber and the solid white line is the GRIN fiber end-face. (c) Measured spot profile at focus at 920 nm. (d) Simulation of the optical intensity evolution at 1300 nm for a GRIN fiber length of 101  $\mu\text{m}$  and (e) measured spot profile at focus at 1300 nm (in air, 64  $\mu\text{m}$  after the GRIN fiber end-face).

diameter of 48  $\mu\text{m}$  and a parabolic refractive index profile with a maximum refractive index difference of  $30 \times 10^{-3}$  between the core center and the cladding. The length of the GRIN fiber segment was optimized through numerical simulations to obtain the smallest achievable MFD at its end-face (*i.e.* smallest focal spot). Numerical simulations were performed using the model of [46]. Fig. 2(b) shows the simulated beam evolution in a 171  $\mu\text{m}$  long GRIN fiber (as measured from the experimental fiber of Fig. 2(a)). The input beam corresponds to the fundamental mode of the hollow-core fiber (24  $\mu\text{m}$  MFD), white dashed lines represent the core/cladding interface of the GRIN fiber and the solid white line is the GRIN fiber end-face. The simulated focal spot has a full width at half maximum (FWHM) of 2.37  $\mu\text{m}$ , located 11  $\mu\text{m}$  away in the air from the GRIN fiber end-face. This is because the theoretical half self-imaging period is 188  $\mu\text{m}$  and the actual GRIN fiber is slightly shorter (171  $\mu\text{m}$ ) due to fabrication uncertainties. The intensity profile measured at focus is displayed in Fig. 2(c). It has a FWHM of 2.4  $\mu\text{m}$ , in excellent agreement with simulations. The 3-photon fiber was designed with a much shorter GRIN fiber tip in order to address the parasitic THG noise issue raised above. Fig. 2(d) shows the beam evolution versus propagation distance for a GRIN fiber length of 101  $\mu\text{m}$ . The focal spot is located 64  $\mu\text{m}$  away from the fiber end-face, which significantly reduces the energy density on the fiber/air interface and the resulting THG. The simulated FWHM of the focused beam is 4.32  $\mu\text{m}$ , in excellent agreement with the measured one of 4.2  $\mu\text{m}$ , displayed in Fig. 2(e).

To summarize, the 2-photon fiber has a 2.4  $\mu\text{m}$  FWHM

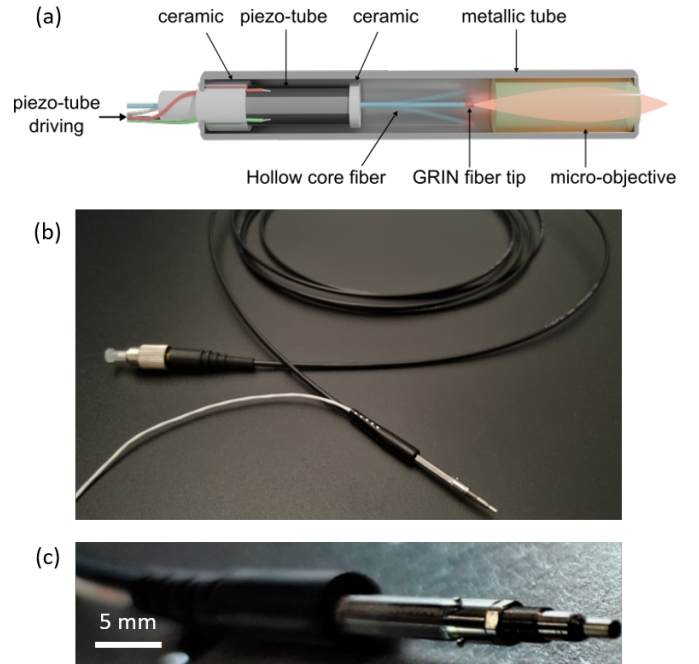


Fig. 3. (a) Scheme of the inside of the distal rigid endoscopic head. Distal head dimensions: 1.3 mm to 2.2 mm in diameter (depending on the micro-objective) and 40 mm in length. Total weight <2 g. (b) Photograph of the whole flexible endoscopic probe (in black the hollow core fiber, in white the scanner control electrical cable terminated with a USB connector (not shown)). (c) Closer zoom of the distal head.

beam located almost on the GRIN fiber end face and the 3-photon fiber has a larger beam size at focus of 4.2  $\mu\text{m}$ , located 64  $\mu\text{m}$  away from the GRIN fiber end-face.

### C. Distal head

Fig. 3(a) shows a sketch of the inside of the distal head. The uncoated end of the hollow core fiber (in blue) is glued into a four quadrant piezo-tube in order to perform a scan. The piezo-tube quadrants are driven by four electrical connections (see details in next Section) and are held into the endoscope metallic tube by two ceramics. The laser beam focused spot formed at the end of the GRIN fiber piece (in red) is re-imaged on the sample with a miniature micro-objective that is integrated in the surrounding metallic tube. We used either a custom micro-objective based on four commercially available achromatic doublets (labeled 4L-MO) or a commercial GRIN micro-objective (GRIN-MO). Their full optical properties as well as the detailed characteristics of the output spot obtained with both fibers is detailed in Section V hereafter. Fig. 3(b) is a photograph of an endoscopic probe, where the white wire is the electrical driving of the piezo-tube terminated with a USB connector (not shown). The proximal side of the endoscope is mounted with a FC/PC connector and the length of the flexible endoscope fiber is typically 2.5 m. Fig. 3(c) is a close-up view of the manufactured distal head that has a diameter of 1.3 mm (with the 4L-MO) and 2.2 mm (with the GRIN-MO) and a rigid length of 40 mm. Its total weight is <2 g. The transmission of the full endoscope was measured to be above 40% in the 920 nm - 1300 nm range.

### III. INTEGRATED RESONANT PIEZO SCANNER AND SPIRAL SCANNING IMAGE ACQUISITION

The functionalized fiber presented in the previous sections is inserted into a piezoelectric tube (Fig. 3) in order to make a spiral scanning trajectory [19], [20], [25], [26], [29], [36]. In this section, we present technical details we have implemented in order to improve the image acquisition.

#### A. Integrated resonant piezo scanner

Fig. 4(a) is an illustration of the signal used to drive the 4 quadrants piezoelectric tube (PT Piezo scanner tubes, PI) in order to obtain a spiral scan. Only the drive voltage along one direction is shown in Fig. 4(a). In the orthogonal direction the drive signal is similar, but with a  $\pi/2$  phase difference which produce a spiral scan as shown in Fig. 4(b). The scanned cycle is composed of a ‘scan time’, which is a sine wave along one axis and a cosine wave along the other axis, both at a frequency equal to the resonant frequency of the free-standing fiber that is attached to the 4-quadrant piezo tube (see Fig. 3). An amplitude modulation is also added during this ‘scan time’ that expands the spiral radius over time (Fig. 4(a), scan time). This is during this ‘scan time’ that the optical signals (2-Photon, SHG, ...) are acquired. The ‘scan time’ ends when the spiral reaches its maximum radius. Then starts the ‘brake time’ where active braking is performed by keeping the resonant drive voltages along the two ( $x, y$ ) piezo axes but with opposite phases to the resonant fiber movement. The reason for this ‘brake time’ is to bring the fiber back to its original position, at the center, as quick as possible before the next ‘scan time’ starts and acquires the next image. An optional ‘rest time’ can also be added to ensure that no residual oscillation is present (Fig. 4(a)).

#### B. Pixel dwell time

The spiral scan (‘scan time’, ‘brake time’, ‘rest time’) requires a proper calibration prior to imaging that is performed in a dedicated calibration step described below. This calibration step is robust enough to be valid during a full day of experiment and has been made automatic to facilitate the operation of the endoscope. We describe below the calibration of the ‘scan time’ which is the most relevant to perform imaging. During the calibration a position sensor detector

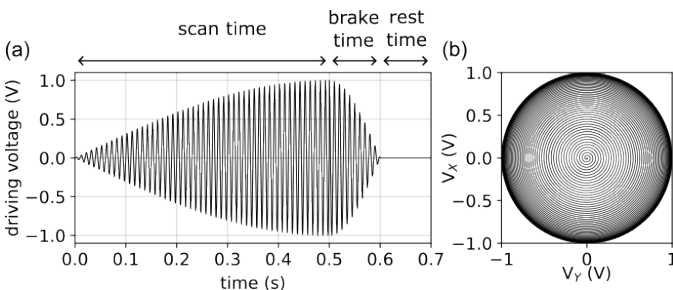


Fig. 4. (a) Excitation signal of one axis corresponding to a full image cycle, including scanning, braking and rest time. (b) Spiral pattern produced by the drive signal during the scan phase.

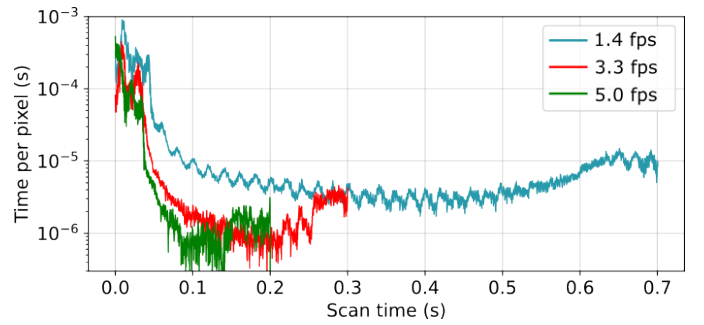


Fig. 5. Pixel dwell time during the scan phase, calculated from experimental  $x(t)$  and  $y(t)$  positions, for different acquisition rates of 1.4 fps (blue line), 3.3 fps (red line) and 5 fps (green line).

(PSD) provides the output position ( $x$  and  $y$ ) of the focused spot at the endoscope image plane as a function of time during the ‘scan time’. The known  $x(t)$  and  $y(t)$  positions are necessary to reconstruct the final image by matching the recorded optical signal (2-photon, SHG,...) with the sample spot position  $x(t)$  and  $y(t)$ . Because the scanner is working at resonance, the time to achieve a circle within the spiral scan is the same whatever the radius in the spiral. This leads to an uneven sampling grid where the center of the image sees the laser beam much longer than the outer part of the FoV. To get some insight into this peculiar scanning scheme we can count the number of data acquisitions corresponding to each image pixel across the FoV. Moreover, we can follow the spiral pattern and match each pixel with the number of acquisitions it contains, thus providing the time spent on each pixel (the pixel dwell time) as a function of time. This is illustrated in Fig. 5. The pixel dwell time is calculated for different acquisition rates of 1.4 fps (blue line), 3.3 fps (red line) and 5 fps (green line). For each acquisition rate investigated, the pixel dwell time is at least two orders of magnitude larger at the beginning of the scan (at the center of the image) as compared to the remaining pixels at latter time. This phenomenon causes photobleaching issues at the center of the image where the sample is over illuminated. This problem is solved in our system using a dedicated power management across the scan.

#### C. Power management

The high power density at the center of the image is inherent to the spiral shape of the resonant scan, and can lead to photobleaching or sample burning, as explained above. An example of photobleaching observed while imaging a fixed retina tissue is exhibited in Fig. 6(a). This can also be evidenced by reconstructing an image with a constant signal (fluoresceine liquid layer) where the center appears very bright (Fig. 6(b)). This image is voluntarily overexposed to allow the weaker signal away from the center to be visible. The plot in Fig. 6(d) is the intensity profile along the dashed line of Fig. 6(b). It shows a very steep peak at the center, emphasizing further this issue. To overcome this problem, we can divide the signal measured by the dwell time calculated above. Applying this to case of Fig. 6(b) leads to the image reconstructed in Fig. 6(c). The plot in Fig 6(e), which is the intensity profile along the dashed line of Fig. 6(c), features an almost flat signal

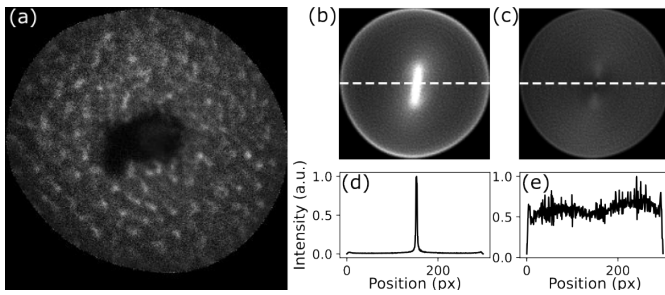


Fig. 6. (a) 3-photon image of a fixed mouse retina sample, showing an example of photobleaching spot at its center. Image of fluoresceine liquid film reconstructed from a typical experimental calibration for (b) a constant signal and (c) a signal adjusted using the time per pixel calculated beforehand. (d) and (e) are intensity plots along dashed lines of (b) and (c) respectively. 1 fps, 100  $\mu\text{m}$  FoV, micro-objective: 4L-MO

in good agreement with the fluoresceine concentration in this test sample. This re-scaling does not avoid the photobleaching at the image center. To solve this problem we have added an acousto-optic modulator (AOM) before injection into the endoscope which controls the excitation laser power over time during the expansion of the spiral scan. By controlling the ramp-up power with increasing image radius acquisition we can make the average power delivered per pixel constant, with this the spiral illumination scheme is not harmful to the sample at the center of the FoV.

In order to illustrate this experimentally, we compare in Fig. 7(c) and (d) 2-photon images of aggregates of fluorescent beads taken without and with a AOM power management respectively. These images were taken with an excitation wavelength of 920 nm, a FoV of 100  $\mu\text{m}$  with the 4L-MO at 1 fps. Without the power management scheme (AOM off), the average power was constant and equal to 39 mW, as shown in Fig. 7(a) displaying its evolution over one scan cycle. The initial image taken in these condition is displayed in Fig. 7(c), and images on the right shows the evolution of its center (delimited by the red frame) over time. Some features initially present within the red circle progressively lose contrast until they completely disappear after 40 s, due to photobleaching. With the power management scheme activated (AOM on), the average power increases exponentially from 0 to 39 mW over one scan cycle, as shown by the plot of Fig. 7(b). The power was also set to 0 during the brake and rest times (see Fig. 4). In this case, the initial image shown in Fig. 7(d) does not deteriorate over time, as shown by the focus on its center (delimited by the red square) over time.

#### D. Image reconstruction

In practice, we found that it is almost impossible for the fiber to be completely immobile after a full image cycle. Some residual movements are always present and affect the subsequent cycle. The result is an uncertainty of the exact position of the fiber at a given time during a multiple image scan. This leads to a visible movement between frame-to-frame images, even though the object imaged is actually static. Such an effect is usually minimal, to the point of being almost invisible, but it can visually affect the images for high repetition rates ( $>5\text{Hz}$ ),

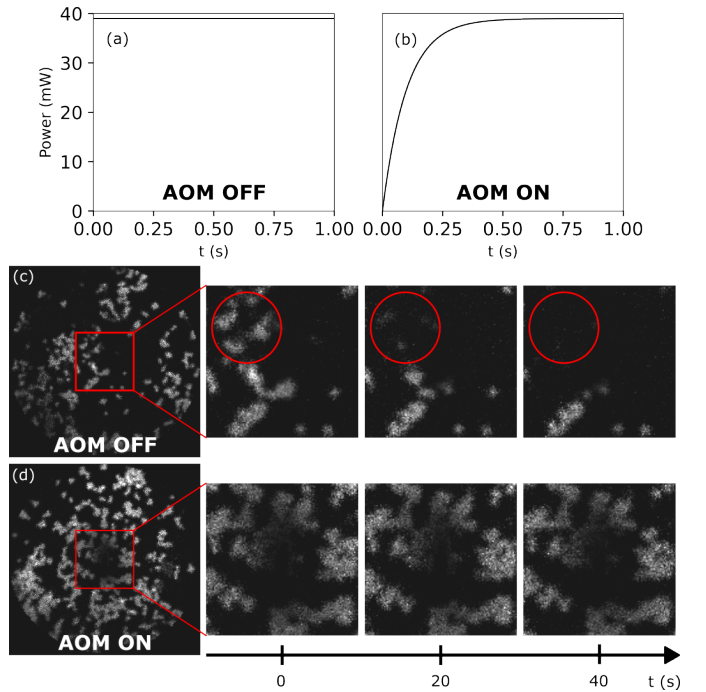


Fig. 7. Evolution of the excitation average power during one scan cycle, which is also the excitation power with increasing radius during the image acquisition, (a) with the AOM off and (b) with the AOM on. 2-photon images of fluorescent beads aggregates (c) with the AOM off and (d) with the AOM on. Right images show the evolution of the image center delimited by the red square over exposition time.

as evidenced by the animation of [Supp info movie 1](#) (left). To circumvent this effect, we developed a motion compensation algorithm based on the open-source module open-cv and using the so-called Demon's algorithm [47]. The real-time algorithm can detect these parasitic movements and compensate for them, as showed in the reconstructed video of [Supp info movie 1](#) (right).

#### E. Control software

All parameters related to scanner parameters and calibration, laser power, as well as image acquisition and processing are controlled from a user-friendly control software. Details and examples of screenshots are provided in Appendix A. This makes the endoscope system easy to use to a non-specialist user and provides stacks of images that can be analyzed with conventional softwares (ImageJ, Suite2P, etc) but also used in user code (MatLab, Python, etc).

## IV. INTEGRATED STAND-ALONE ENDOSCOPE RACK

The whole endoscope and its control units are racked in a movable cabinet as shown in Fig. 8(a). The stand-alone multiphoton endoscope system contains a compact and rackable femtosecond fiber laser. In the present study, it is a 920 nm,  $>1.5\text{ W}$ , 80 MHz,  $<100\text{ fs}$  pulse duration laser (Femto Fiber ultra 920, Toptica). The control electronics required to drive the piezo scanner and the control computer are also included in the cabinet. The monitor and keyboard are included *via* a movable arm attached to the side. The cabinet also contains two

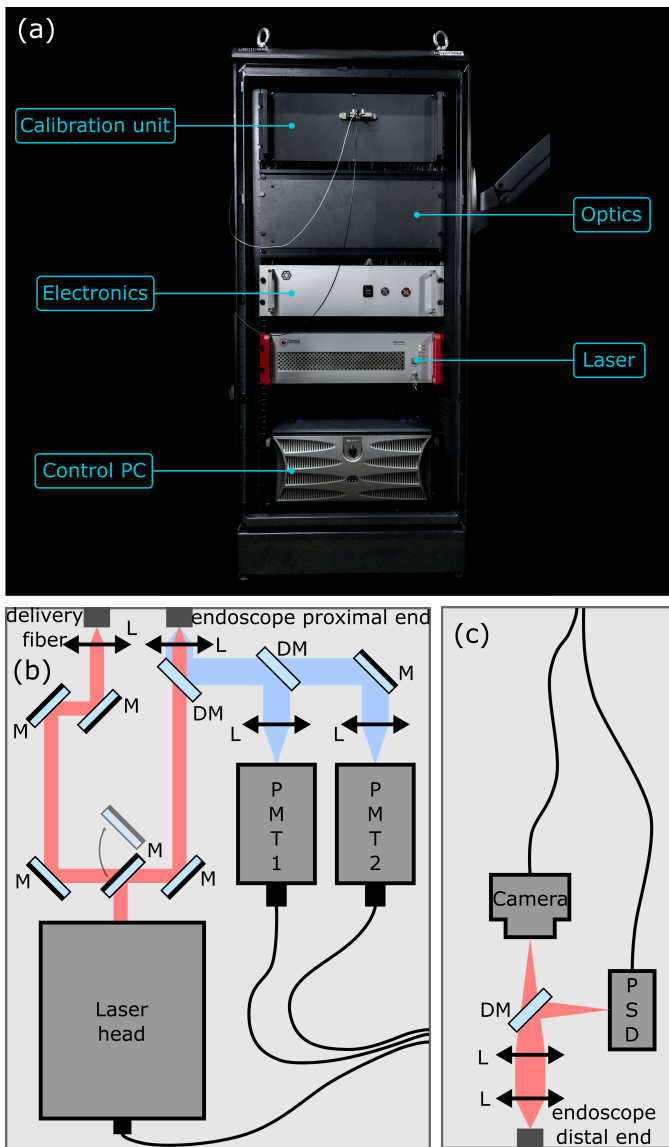


Fig. 8. (a) Picture of the endoscope integrated cabinet. (b) Scheme of the optical 'coupling/detection unit'. The excitation laser can be a laser head integrated into the endoscope kart or coming from a delivery fiber (see section VII). (c) Scheme of the 'calibration unit'. L: lens ; M: mirror ; DM: dichroic mirror ; PMT: photomultiplier tube.

optical units. The first one, represented in Fig. 8(b), contains a coupling stage required to inject light from the laser source into the endoscope hollow core fiber, either directly from the fiber laser head integrated into the cabinet, or from a laser located outside the rack using a dedicated hollow core delivery fiber (see section below). A flipping mirror located inside the unit allows to switch between these two configurations (internal or external lasers). The nonlinear signal (2-photon, SHG,...) collected from the sample is separated from the excitation laser by a dichroic mirror, and two photomultiplier detectors can be placed to simultaneously detect two nonlinear signals depending on the filters applied.

The second optical unit displayed in Fig. 8(c) is the 'calibration unit'. As mentioned before this is mandatory to record the spiral focus point trajectory of the 'scan time'. For that the

distal head of the endoscope is directly plugged to the front of the integrated cabinet and the moving focused spot at the endoscope distal side is imaged onto both a camera and a PSD. The camera is used to adjust the injection into the hollow core fiber and the PSD records the positions  $(x(t), y(t))$  of the spot during the scan. It allows to map the shape of the spiral scan and adjust the driving voltage parameters to obtain the most symmetric and extended spiral pattern that directly defined the endoscope FoV. This  $(x(t), y(t))$  calibration is required to reconstruct images during live acquisition as positions are attributed to each intensity measured, thus allowing to fill each pixel of the image with the appropriate measured intensity. Typically the endoscope can image a FoV of  $600 \mu\text{m}$  at a maximum of 10 fps. The transmission of the full endoscope system is typically above 40% that provides sufficient power to perform nonlinear imaging using a  $>1 \text{ W}$  laser system.

## V. IMAGING PERFORMANCES

The endoscope distal head (Fig. 3) can be assembled either with the 2-photon or the 3-photon fiber described in section II B. In each case, two different micro-objectives can be used. The first one is a micro-objective based on four commercially available achromatic doublets (4L-MO) with a theoretical magnification of 0.63, a NA of 0.3 on the fiber side and 0.45 on the sample side and a working distance (WD) of  $600 \mu\text{m}$  in air. The second one is a commercially available GRIN micro-objective (GRIN-MO) (GT-MO-070-016-ACR-VISNIR-30-20, GRINTECH) with a magnification of 0.22, a NA of 0.16 on the fiber side and 0.7 on the sample side and a WD of  $230 \mu\text{m}$  in air.

The choice between these two micro-objectives depends on the expected performances and desired imaging modality which are summarized in Table I. For example, because of their different magnification, they provide different FoV. Thus, the maximal FoV obtainable experimentally with negligible distortions is  $600 \mu\text{m}$  with the 4L-MO and  $225 \mu\text{m}$  with the GRIN-MO.

Table I also summarizes measurements of the lateral and axial point spread function (PSF), corresponding to the lateral and axial resolution, for each imaging modality. The 2-photon and 3-photon PSF measurements were performed using 200

TABLE I  
SUMMARY OF THE OPTICAL PERFORMANCES OF THE TWO MICRO-OBJECTIVES WITH OPTIMIZED PROBES. \*MEASURED WITH THE 2-PHOTON FIBER. \*\*MEASURED WITH THE 3-PHOTON FIBER.

MO type	4L-MO		GRIN-MO	
	Lateral	Axial	Lateral	Axial
WD ( $\mu\text{m}$ )	$600 \pm 15$		$230 \pm 15$	
Max FoV ( $\mu\text{m}$ )	600		225	
2-photon PSF ( $\mu\text{m}$ )*	1.37	10.90	1.12	11.64
SHG PSF ( $\mu\text{m}$ )*	1.53	12.00	1.00	10.16
3-photon PSF ( $\mu\text{m}$ **)	1.77	16.16	1.49	3.75
THG PSF ( $\mu\text{m}$ **)	1.42	14.39	1.62	4.93

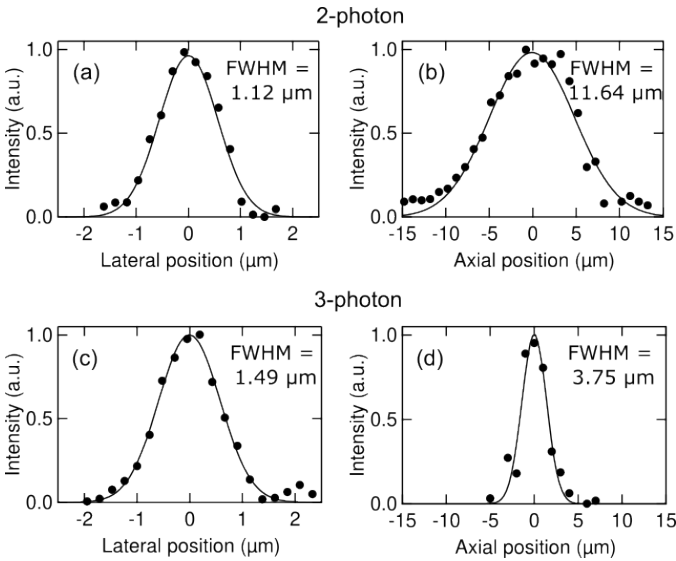


Fig. 9. Measurement of the 2-photon and 3-photon spatial resolution with the GRIN-MO. (a) 2-photon lateral and (b) axial PSF measured with the 2-photon fiber at 920 nm. (c) 3-photon lateral and (d) axial PSF measured with the 3-photon fiber at 1300 nm. Markers are experimental data and solid lines are Gaussian fits.

nm diameter fluorescent beads diluted in water and placed between slide and slip cover. The measurement of the SHG PSF was done using KTP nanocrystals of  $150 \pm 100$  nm diameter diluted and placed between a poly-D-Lysine coated coverslip and a slide [48]. For the THG resolution measurement, we imaged a silicon integrated ring resonator waveguide of 450 nm width embedded in an oxide cladding [33]. In each case, the lateral resolution corresponds to the FWHM value of the Gaussian fit of the image. The axial resolution was obtained from a Gaussian fit of the evolution of the maximum nonlinear signal while the endoscope is moved in the axial direction.

The 2-photon and 3-photon lateral and axial resolution measurements obtained with the GRIN-MO are illustrated in Fig. 9. Figs. 9 (a) and (b) show respectively the lateral and axial 2-photon PSF measurement performed with the GRIN-MO and the 2-photon fiber. The 2-photon lateral and axial resolution are respectively  $1.12 \mu\text{m}$  and  $11.64 \mu\text{m}$ . Figs. 9 (c) and (d) displays respectively the lateral and axial 3-photon PSF measured with the 3-photon probe, which are found to be  $1.49 \mu\text{m}$  and  $3.75 \mu\text{m}$  respectively. Similar measurements were done with the 4L-MO, as well as in SHG and THG modalities with both micro-objectives. The measurements are not shown here for the sake of clarity, but all results are summarized in Table I.

As expected, the GRIN-MO offers improved spatial resolution with regards to the 4L-MO, at the expense of a  $\sim 3$  times smaller WD and FoV. Remarkably, the axial resolution measured with the GRIN-MO in 3-photon and THG modalities are significantly better than in 2-photon and SHG. The effective focal volume [49] is  $4.36 \mu\text{m}^3$  in 3-photon imaging modality and  $6.78 \mu\text{m}^3$  in THG.

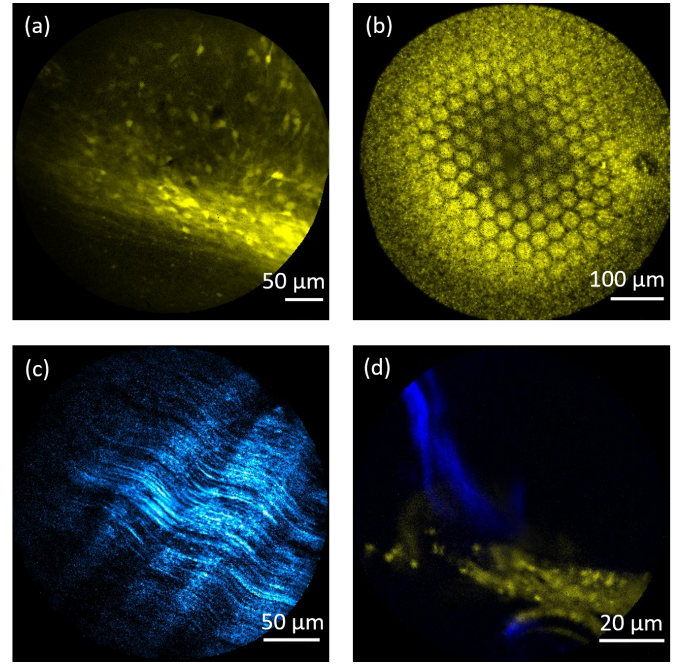


Fig. 10. (a) 2-photon image of fixed mouse brain. (b) 2-photon image of unlabeled insect cornea. (c) SHG image of yellow elastic connective tissue. (d) composite 2-photon (yellow) and SHG (blue) image of rat peritoneum. See acquisition details in the text.

## VI. IMAGING WITH THE BUILT-IN FS LASER

In order to test the imaging ability of our system, we performed a first round of experiments on various biological tissues using the fully integrated kart. The laser used is the 920 nm fs fiber laser although 780 nm (1 W) and 1050 nm (5 W) fs lasers are also available. This was done using the 2-photon fiber associated with either the 4L-MO or GRIN-MO.

### A. Tissue samples

Fig. 10 shows a collection of images taken with the flexible endoscope system on different biological samples. Fig. 10(a) shows a 2-photon image taken on a fixed mouse brain labelled with GFP proteins (FoV  $416 \mu\text{m}$ , 1 fps, average power at the sample 65 mW, 4L-MO). It highlights neurons in the hippocampus. Fig. 10(b) is a 2-photon image of fixed unlabeled insect cornea showing the surface of many ommatidia (FoV  $600 \mu\text{m}$ , 10 fps, 17 mW power, 4L-MO). Fig. 10(c) is a SHG image of fixed yellow elastic connective tissue showing collagen fibrils structures (FoV  $280 \mu\text{m}$ , 1.4 fps, 25 mW power, 4L-MO). Fig. 10(d) is a multimodal 2-photon (yellow) and SHG (blue) image of fixed rat peritoneum showing the elastin and collagen (FoV  $98 \mu\text{m}$ , 1 fps, 25 mW power, GRIN-MO).

### B. Plant samples

Next we tested the endoscope system for plant imaging, with some examples displayed in Fig. 11. Fig. 11(a) shows a 2-photon image of fixed marram grass (*ammophila arenaria*) leaf stained with iodine green carmine stain (FoV  $500 \mu\text{m}$ , 1.4 fps, power 20 mW, 4L-MO). Yellow parts correspond to the 2-photon fluorescence filtered at  $630 \pm 46$  nm and green parts are



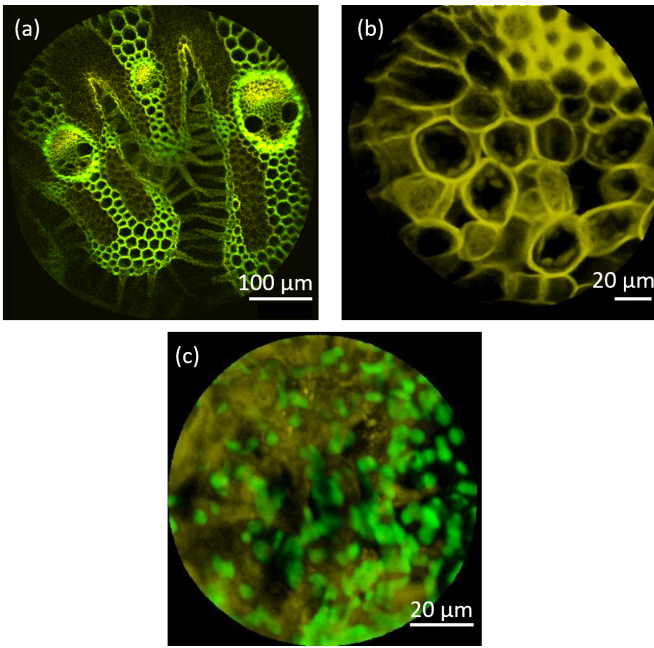


Fig. 11. 2-photon images of (a) stained marram grass (*ammophila arenaria*) leaf at 520 nm (green) and 630 nm (yellow), (b) of stained holly (*ilex aquifolium*) leaf and (c) 2-photon auto-fluorescence of fresh orchid leaf at 520 nm (yellow) and 630 nm (green). See acquisition details in the text.

taken at  $520 \pm 30$  nm. Folded structures used to trap water and vascular bundles typical of *ammophila arenaria* leaves can be seen. Fig. 11(b) is a 2-photon image of holly (*ilex aquifolium*) leaf stained with lugol's iodine (FoV of 168  $\mu$ m, 1 fps, 20 mW, GRIN-MO, detection filter  $520 \pm 30$  nm). The system can also be used to study 2-photon auto-fluorescence and Fig. 11(c) is a 2-photon image of a fresh orchid leaf taken directly in a plant pot. Lignin is shown in yellow (acquired with a  $520 \pm 30$  nm filter) and chlorophyll in green with a  $630 \pm 46$  nm filter (FoV of 98  $\mu$ m, 1 fps, 20 mW, GRIN-MO).

### C. In vivo imaging

The manipulation of the distal head is easy to perform *in vivo* imaging. As an example, Fig. 12 shows a 2-photon auto-fluorescence image of human skin taken by manually holding the endoscope housed in a pen-like accessory in one hand and

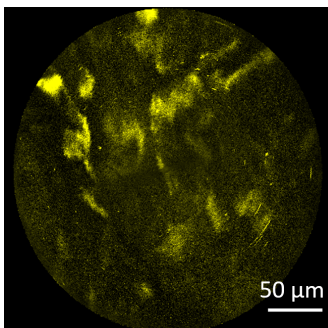


Fig. 12. 2-photon autofluorescence live imaging of human skin by holding manually the endoscope housed in the dedicated pen-like accessory directly onto the forearm.

moving either its integrated miniature translation stage to find the signal, or sweeping the endoscope on the skin with the other hand (FoV 300  $\mu$ m, 6 fps, 70 mW power, 4L-MO). The corneocytes from the stratum corneum can be identified. [Supp info movie 2](#) shows a handheld holder where the endoscope distal head has been inserted to facilitate its manipulation and manual focusing for *in vivo* imaging.

## VII. IMAGING USING THE DELIVERY FIBER

As mentioned above the stand-alone endoscope system can handle fs fiber laser systems at 920 nm, 780 nm and 1050 nm whose small footprints enable their integration into the endoscope kart. These  $\sim 100$  fs, 80 MHz laser repetition rate are suitable for 2-photon, SHG and possibly (1050 nm) THG imaging. However, there are situations where more energetic pulses are required such as for 3-photon and THG imaging. Typically 3-photon requires lower repetition rate  $\sim 1$  MHz and much shorter  $\sim 50$  fs pulses at a typical wavelength of 1300 nm. Such energetic ( $\sim \mu$ J) pulses can only be obtained from high-power oscillators pumping massive optical parametric amplifiers (OPAs). These laser systems are currently only available in a table-top format and cannot be integrated in a movable system. In order to use the stand-alone kart integrated endoscope system for 3-photon and THG imaging, we developed a 'delivery fiber' whose function is to deliver ultrashort pulses from a table-top laser system into the optical coupling unit of the endoscope kart (see Fig. 8(b)). The delivery fiber is a negative curvature hollow core fiber similar to the one presented in Fig. 1, except that it has a high-index polymer coating so that it does not have a double-clad. The delivery fiber enters the endoscope optical unit as shown in Fig 8(b) and a flip mirror (shown in Fig 8b) can couple the rack-integrated laser beam or the light coming from the delivery fiber to the endoscope flexible fiber. The transmission of the delivery fiber was measured to be 75% across the 940 nm - 1300 nm range, this fulfils most of the requirements to bring table-top large frame multiphoton lasers into the endoscope. Fig. 13 shows a scheme of the experimental setup: a table-top laser system composed of a pump oscillator and an OPA is placed on an optical table. The laser beam is coupled into the delivery fiber

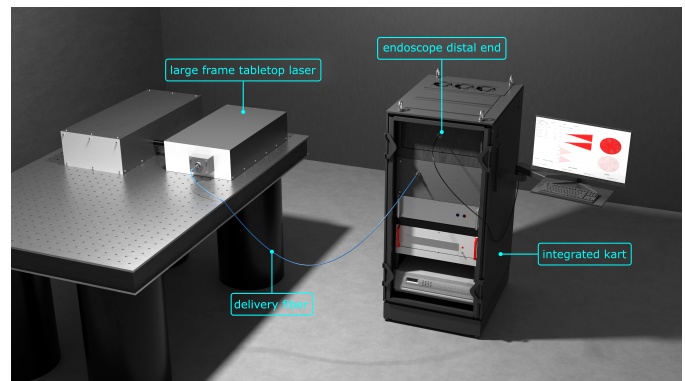


Fig. 13. View of the delivery fiber scheme: a large frame table top laser light beam is brought into the endoscope kart system using the hollow core delivery fiber.

whose output is plugged on the input port of the stand-alone kart.

### A. 3-photon

To perform 3-photon imaging we use an ytterbium-doped master oscillator power amplifier Monaco-1035 (Coherent) pumping and optical parametric amplifier (Opera-F, Coherent) that delivers 2.5 W of average power at 1300 nm and 940 nm with a 1 MHz repetition rate and  $\sim 50$  fs pulse duration. We use 100 mW of the OPA beam to get 75 mW at the delivery fiber output (fiber delivery transmission: 75% ) that ended up to 30 mW at the endoscope distal side (endoscope transmission: 40%). Figure 14 (a) shows 3-photon fluorescence (excitation: 940 nm, detection: 433 nm) of a DAPI (4',6-diamidino-2-phenylindol) stained epithelium pig retina whereas Figure 14 (b) shows the endothelial of the same. Corneal button was carefully separated from the rest of the eyeball sample, stained with 10  $\mu\text{g}/\text{mL}$  Hoechst 33342 solution in PBS for 5 min and rinsed in PBS without further fixation. Corneal button was directly placed in direct contact with a 35 mm glass bottom dish before observation. In both epithelium and endothelial parts the cell nuclei can be easily distinguished (FoV 98  $\mu\text{m}$ , 1 fps, 30 mW average power, GRIN-MO).

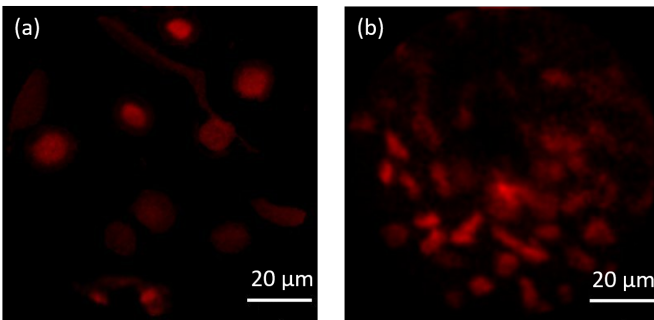


Fig. 14. 3-photon image of a DAPI stained pig retina (a) epithelium, (b) endothelium. See acquisition parameters in text.

### B. Multimodal imaging

Using the built-in PMT detectors, the endoscope system can perform multi-color multimodal imaging.

Figure 15 (a) shows a 3-photon fluorescence (fluo:  $520\pm 30$  nm) and THG (detection:  $433\pm 20$  nm) image of a human brain section stained with hematoxylin and eosin and excited at 1300 nm (FoV 168  $\mu\text{m}$ , 1 fps, 15 mW power, GRIN-MO). The fluorescence comes from the eosin stain whereas the THG might come from nucleoli. Figure 15 (b) shows a 3-photon fluorescence (red) (fluo:  $520\pm 30$  nm), SHG (green) (detection:  $650\pm 30$  nm) and THG (blue) (detection:  $433\pm 20$  nm) image of a fixed de-fatted human adipocyte tissue stained with Masson's trichrome (Nublac commercial stained slides) and excited at 1300 nm (FoV 168  $\mu\text{m}$ , 1 frame/s, 15 mW power, GRIN-MO). Fluorescence reveals the adipocyte border whereas SHG reveals collagen fibers and THG small vesicles.

These images illustrate some of the imaging capabilities of the endoscope but some others could be added such as CARS [26], [29].

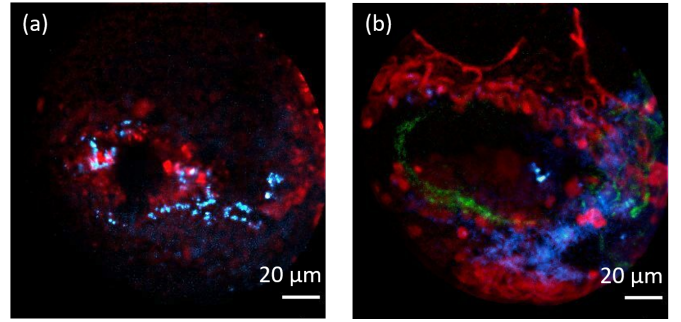


Fig. 15. Multimodal imaging. (a) Composite 3-photon (red) and THG (blue) image of a human brain section stained with hematoxylin and eosin. (b) 3-photon (red), SHG (green) and THG (blue) image of a fixed de-fatted human adipocyte tissue stained with Masson's trichrome. See acquisition details in text.

## VIII. CONCLUSION

We have presented a flexible endoscope system based on a double-clad hollow core fiber that enables to perform nonlinear imaging over a broad range of near infrared excitation wavelengths. We have demonstrated 2-photon/SHG imaging using a 920 nm, 100 fs laser and 3-photon/THG imaging using a 1300 nm, 50 fs high power laser system. Quite remarkably, the double-clad hollow core fiber can handle a broad range of excitation wavelength still maintaining the fs short pulse duration while the nonlinear signal is efficiently collected through the 0.38 NA double-cladding. The endoscope head as a distal diameter of 2.2 mm using the four lenses micro-objective (4L-MO) and 1.3 mm using the GRIN micro-objective (GRIN-MO) and can image across a FoV up to 600  $\mu\text{m}$  at a maximum of 10 fps and with a  $\sim 1$   $\mu\text{m}$  spatial resolution (depending on the micro-objective - see Table I). The small endoscope head (weight  $< 2$  g,  $\leq 2.2$  mm diameter, 40 mm length) can be easily manipulated to access hard-to-reach places and we have demonstrated its handheld manipulation to image the skin forearm *in vivo*. It could be also readily used for *in vivo* brain activity monitoring in mice [50]. The endoscope could be further improved by adding a  $z$  scanner to the 2D resonant piezo scanner using small memory alloy actuators [51], [52]. A unique feature brought by the weak nonlinearity of the hollow core fiber endoscope is its ability to activate nonlinear contrasts that involve overlapping pulses such as SRS [53] and CARS [26]. We expect the endoscope to find a broad range of applications in the fields of biology, material sciences and medical applications as being a valuable miniature extension of bulky multiphoton microscopes.

## ACKNOWLEDGMENTS

We acknowledge financial support from the French National Research Agency (ANR-19-CE19-0019-03 MEAP, ANR-10-INSB-04-01, ANR-11-INSB-0006, ANR-16-CONV-0001, ANR-21-ESRS-0002 IDEC), the Contrats de Plan Etat-Region (CPER WaveTech), the French Ministry of Higher Education and Research, the Centre National de la Recherche Scientifique (CNRS), the Hauts-de-France (HdF) Regional Council, the European Regional Development Fund (ERDF), IRCICA. We also acknowledge Rabei Mohammadi and Thierry Gacoin

(Ecole Polytechnique) for providing the KTP nanocrystals used for SHG resolution measurement and Bart Kuyken (UGent-IMEC) for providing the silicon ring resonator waveguide used for THG resolution measurement. The authors acknowledge Marie-Claire Schanne-Klein (Ecole Polytechnique), Esben Andresen (PhLAM) and Siddarth Sivankutty (PhLAM) for fruitful discussions.

CONFLICT OF INTEREST

H.R. and A.K. declare they have interest in the activity of Lightcore Technologies.

APPENDIX A  
SOFTWARE

Fig. B shows some screenshots of the control endoscope software that has been developed to drive the stand-alone flexible endoscope system. In particular, it allows: to control the FoV, correct the dwell time issue, modulate the laser power to mitigate photobleaching, measure the signal in real-time, acquire and save images, perform image and video processing, color the images, adjustment the contrast, perform local motion correction, and fill blank pixels. It also performs the scanner calibration and allows to pre-record several calibrations.

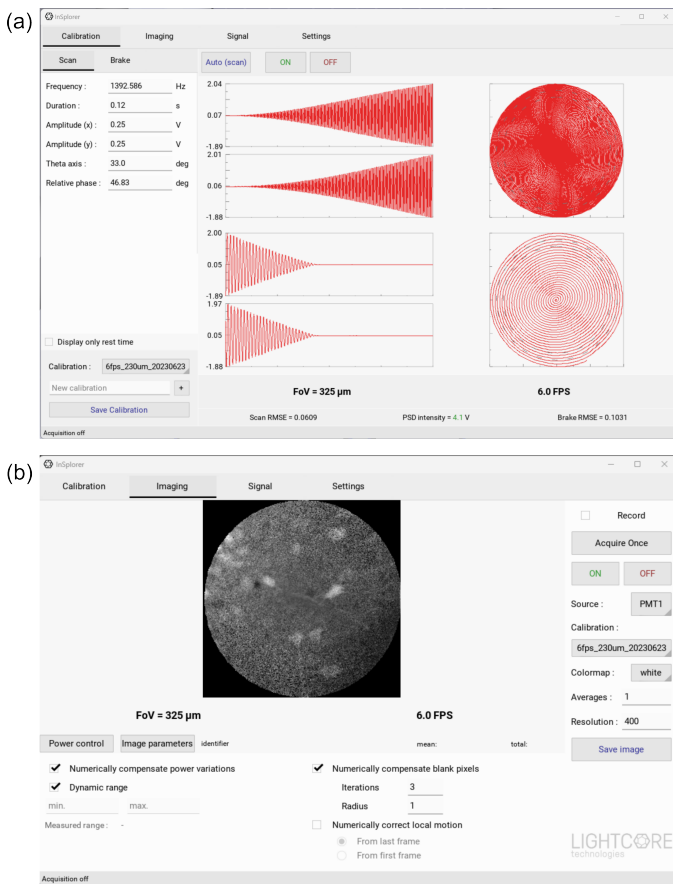


Fig. 16. Screenshots of the custom control endoscope software showing the (a) 'calibration screen' with the scanner trajectories and the (b) 'imaging screen' with live-processing options.

APPENDIX B  
IN VIVO ENDOSCOPIC IMAGING

In order to highlight the potential of performing *in vivo* endoscopic imaging using the system, we provide movies of *in vivo* 2-photon autofluorescence taken inside the mouth. [Supp info movie 3](#) and [Supp info movie 4](#) correspond respectively to the inside of the cheek and to the tongue of one of the co-authors. They were taken using a 860 nm laser (200 fs, 80 MHz) injected into the delivery fiber presented in the text and then injected into the movable kart. The movies were acquired at 6 fps, with a FoV of 120 μm and an average power of 50 mW using the GRIN-MO. The distal head of the endoscope was mounted on the pen-like accessory which can be seen in [Supp info movie 2](#). These videos show cellular features that cannot be acquired *in vivo* with bench top microscopes.

REFERENCES

- [1] W. R. Zipfel, R. M. Williams, R. Christie, A. Y. Nikitin, B. T. Hyman, and W. W. Webb, "Live Tissue Intrinsic Emission Microscopy Using Multiphoton-Excited Native Fluorescence and Second Harmonic Generation," *Proceedings of the National Academy of Sciences of the United States of America*, vol. 100, no. 12, pp. 7075–7080, 2003, publisher: National Academy of Sciences. [Online]. Available: <https://www.jstor.org/stable/3139434>
- [2] C. J. R. Sheppard, "Multiphoton microscopy: a personal historical review, with some future predictions," *Journal of Biomedical Optics*, vol. 25, no. 1, p. 014511, Jan. 2020, publisher: SPIE. [Online]. Available: <https://www.spiedigitallibrary.org/journals/journal-of-biomedical-optics/volume-25/issue-1/014511/Multiphoton-microscopy--a-personal-historical-review-with-some-future/10.1117/1.JBO.25.1.014511.full>
- [3] R. Carriles, D. N. Schafer, K. E. Sheetz, J. J. Field, R. Cisek, V. Barzda, A. W. Sylvester, and J. A. Squier, "Invited Review Article: Imaging techniques for harmonic and multiphoton absorption fluorescence microscopy," *Review of Scientific Instruments*, vol. 80, no. 8, p. 081101, Aug. 2009. [Online]. Available: <https://doi.org/10.1063/1.3184828>
- [4] D. R. Miller, J. W. Jarrett, A. M. Hassan, and A. K. Dunn, "Deep tissue imaging with multiphoton fluorescence microscopy," *Current Opinion in Biomedical Engineering*, vol. 4, pp. 32–39, Dec. 2017. [Online]. Available: <https://www.sciencedirect.com/science/article/pii/S2468451117300466>
- [5] A. Diaspro, P. Bianchini, G. Vicidomini, M. Faretta, P. Ramoino, and C. Usai, "Multi-photon excitation microscopy," *BioMedical Engineering OnLine*, vol. 5, no. 1, p. 36, Jun. 2006. [Online]. Available: <https://doi.org/10.1186/1475-925X-5-36>
- [6] H. Ranawat, S. Pal, and N. Mazumder, "Recent trends in two-photon auto-fluorescence lifetime imaging (2P-FLIM) and its biomedical applications," *Biomedical Engineering Letters*, vol. 9, no. 3, pp. 293–310, Aug. 2019.
- [7] A. Aghigh, S. Bancelin, M. Rivard, M. Pinsard, H. Ibrahim, and F. Légaré, "Second harmonic generation microscopy: a powerful tool for bio-imaging," *Biophysical Reviews*, vol. 15, no. 1, pp. 43–70, Feb. 2023.
- [8] B. Weigelin, G.-J. Bakker, and P. Friedl, "Third harmonic generation microscopy of cells and tissue organization," *Journal of Cell Science*, vol. 129, no. 2, pp. 245–255, Jan. 2016.
- [9] W. Min, S. Lu, M. Rueckel, G. R. Holtom, and X. S. Xie, "Near-Degenerate Four-Wave-Mixing Microscopy," *Nano Letters*, vol. 9, no. 6, pp. 2423–2426, Jun. 2009, publisher: American Chemical Society. [Online]. Available: <https://doi.org/10.1021/nl901101g>
- [10] W. Min, C. W. Freudiger, S. Lu, and X. S. Xie, "Coherent Nonlinear Optical Imaging: Beyond Fluorescence Microscopy," *Annual Review of Physical Chemistry*, vol. 62, no. 1, pp. 507–530, 2011, \_eprint: <https://doi.org/10.1146/annurev.physchem.012809.103512>. [Online]. Available: <https://doi.org/10.1146/annurev.physchem.012809.103512>
- [11] H. Rigneault and P. Berto, "Tutorial: Coherent Raman light matter interaction processes," *APL Photonics*, vol. 3, no. 9, p. 091101, Jul. 2018. [Online]. Available: <https://doi.org/10.1063/1.5030335>

- [12] M. C. Fischer, J. W. Wilson, F. E. Robles, and W. S. Warren, "Invited Review Article: Pump-probe microscopy," *Review of Scientific Instruments*, vol. 87, no. 3, p. 031101, Mar. 2016. [Online]. Available: <https://doi.org/10.1063/1.4943211>
- [13] H. Ishii, K. Otomo, T. Takahashi, K. Yamaguchi, and T. Nemoto, "Focusing new light on brain functions: multiphoton microscopy for deep and super-resolution imaging," *Neuroscience Research*, vol. 179, pp. 24–30, Jun. 2022. [Online]. Available: <https://www.sciencedirect.com/science/article/pii/S0168010221002455>
- [14] K. König, "Multiphoton microscopy in life sciences," *Journal of Microscopy*, vol. 200, no. 2, pp. 83–104, 2000, eprint: <https://onlinelibrary.wiley.com/doi/pdf/10.1046/j.1365-2818.2000.00738.x>. [Online]. Available: <https://onlinelibrary.wiley.com/doi/abs/10.1046/j.1365-2818.2000.00738.x>
- [15] B.-G. Wang, K. König, and K.-J. Halbhauer, "Two-photon microscopy of deep intravital tissues and its merits in clinical research," *Journal of Microscopy*, vol. 238, no. 1, pp. 1–20, 2010, eprint: <https://onlinelibrary.wiley.com/doi/pdf/10.1111/j.1365-2818.2009.03330.x>. [Online]. Available: <https://onlinelibrary.wiley.com/doi/abs/10.1111/j.1365-2818.2009.03330.x>
- [16] D. A. Orringer, B. Pandian, Y. S. Niknafs, T. C. Hollon, J. Boyle, S. Lewis, M. Garrard, S. L. Hervey-Jumper, H. J. L. Garton, C. O. Maher, J. A. Heth, O. Sagher, D. A. Wilkinson, M. Snuderl, S. Venneti, S. H. Ramkissoon, K. A. McFadden, A. Fisher-Hubbard, A. P. Lieberman, T. D. Johnson, X. S. Xie, J. K. Trautman, C. W. Freudiger, and S. Camelo-Piragua, "Rapid intraoperative histology of unprocessed surgical specimens via fibre-laser-based stimulated Raman scattering microscopy," *Nature Biomedical Engineering*, vol. 1, no. 2, pp. 1–13, Feb. 2017, number: 2 Publisher: Nature Publishing Group. [Online]. Available: <https://www.nature.com/articles/s41551-016-0027>
- [17] S. Yue, M. Slipchenko, and J.-X. Cheng, "Multimodal nonlinear optical microscopy," *Laser & Photonics Reviews*, vol. 5, no. 4, pp. 496–512, 2011, eprint: <https://onlinelibrary.wiley.com/doi/pdf/10.1002/lpor.201000027>. [Online]. Available: <https://onlinelibrary.wiley.com/doi/abs/10.1002/lpor.201000027>
- [18] S. Tang, W. Jung, D. McCormick, T. Xie, J. Su, Y.-C. Ahn, B. J. Tromberg, and Z. Chen, "Design and implementation of fiber-based multiphoton endoscopy with microelectromechanical systems scanning," *Journal of biomedical optics*, vol. 14, no. 3, p. 034005, 2009. [Online]. Available: <https://www.ncbi.nlm.nih.gov/pmc/articles/PMC2866630/>
- [19] M. T. Myaing, D. J. MacDonald, and X. Li, "Fiber-optic scanning two-photon fluorescence endoscope," *Optics Letters*, vol. 31, no. 8, pp. 1076–1078, Apr. 2006, publisher: Optica Publishing Group. [Online]. Available: <https://opg.optica.org/ol/abstract.cfm?uri=ol-31-8-1076>
- [20] D. Do, H. Yoo, and D.-G. Gweon, "Fiber-optic raster scanning two-photon endomicroscope using a tubular piezoelectric actuator," *Journal of Biomedical Optics*, vol. 19, no. 6, p. 066010, Jun. 2014.
- [21] D. R. Rivera, C. M. Brown, D. G. Ouzounov, W. W. Webb, and C. Xu, "Use of a lensed fiber for a large-field-of-view, high-resolution, fiber-scanning microendoscope," *Optics Letters*, vol. 37, no. 5, pp. 881–883, Mar. 2012, publisher: Optica Publishing Group. [Online]. Available: <https://opg.optica.org/ol/abstract.cfm?uri=ol-37-5-881>
- [22] A. Lukic, S. Dochow, H. Bae, G. Matz, I. Latka, B. Messerschmidt, M. Schmitt, and J. Popp, "Endoscopic fiber probe for nonlinear spectroscopic imaging," *Optica*, vol. 4, no. 5, pp. 496–501, May 2017, publisher: Optica Publishing Group. [Online]. Available: <https://opg.optica.org/optical/abstract.cfm?uri=optica-4-5-496>
- [23] Y. Wu, Y. Leng, J. Xi, and X. Li, "Scanning all-fiber-optic endomicroscopy system for 3D nonlinear optical imaging of biological tissues," *Optics Express*, vol. 17, no. 10, pp. 7907–7915, May 2009, publisher: Optica Publishing Group. [Online]. Available: <https://opg.optica.org/oe/abstract.cfm?uri=oe-17-10-7907>
- [24] K. Murari, Y. Zhang, S. Li, Y. Chen, M.-J. Li, and X. Li, "Compensation-free, all-fiber-optic, two-photon endomicroscopy at 1.55  $\mu\text{m}$ ," *Optics Letters*, vol. 36, no. 7, pp. 1299–1301, Apr. 2011, publisher: Optica Publishing Group. [Online]. Available: <https://opg.optica.org/ol/abstract.cfm?uri=ol-36-7-1299>
- [25] G. Ducourthial, P. Leclerc, T. Mansuryan, M. Fabert, J. Brevier, R. Habert, F. Braud, R. Batrin, C. Veveř-Bizet, G. Bourghackly, L. Thiberville, A. Druilhe, A. Kudlinski, and F. Louradour, "Development of a real-time flexible multiphoton microendoscope for label-free imaging in a live animal," *Scientific Reports*, vol. 5, no. 1, p. 18303, Dec. 2015, number: 1 Publisher: Nature Publishing Group. [Online]. Available: <https://www.nature.com/articles/srep18303>
- [26] A. Lombardini, V. Mytskaniuk, S. Sivankutty, E. R. Andresen, X. Chen, J. Wenger, M. Fabert, N. Joly, F. Louradour, A. Kudlinski, and H. Rigneault, "High-resolution multimodal flexible coherent Raman endoscope," *Light: Science & Applications*, vol. 7, no. 1, p. 10, May 2018, number: 1 Publisher: Nature Publishing Group. [Online]. Available: <https://www.nature.com/articles/s41377-018-0003-3>
- [27] A. Kudlinski, A. Cassez, O. Vanvincq, D. Septier, A. Pastre, R. Habert, K. Baudelle, M. Douay, V. Mytskaniuk, V. Tsvirkun, H. Rigneault, and G. Bouwmans, "Double clad tubular anti-resonant hollow core fiber for nonlinear microendoscopy," *Optics Express*, vol. 28, no. 10, pp. 15 062–15 070, May 2020, publisher: Optica Publishing Group. [Online]. Available: <https://opg.optica.org/oe/abstract.cfm?uri=oe-28-10-15062>
- [28] E. Pshenay-Severin, H. Bae, K. Reichwald, G. Matz, J. Bierlich, J. Kobelke, A. Lorenz, A. Schwuchow, T. Meyer-Zedler, M. Schmitt, B. Messerschmidt, and J. Popp, "Multimodal nonlinear endomicroscopic imaging probe using a double-core double-clad fiber and focus-combining micro-optical concept," *Light: Science & Applications*, vol. 10, no. 1, p. 207, Oct. 2021, number: 1 Publisher: Nature Publishing Group. [Online]. Available: <https://www.nature.com/articles/s41377-021-00648-w>
- [29] D. Septier, V. Mytskaniuk, R. Habert, D. Labat, K. Baudelle, A. Cassez, G. Brévalle-Wasilewski, M. Conforti, G. Bouwmans, H. Rigneault, and A. Kudlinski, "Label-free highly multimodal nonlinear endoscope," *Optics Express*, vol. 30, no. 14, pp. 25 020–25 033, Jul. 2022, publisher: Optica Publishing Group. [Online]. Available: <https://opg.optica.org/oe/abstract.cfm?uri=oe-30-14-25020>
- [30] D. Y. Kim, K. Hwang, J. Ahn, Y.-H. Seo, J.-B. Kim, S. Lee, J.-H. Yoon, E. Kong, Y. Jeong, S. Jon, P. Kim, and K.-H. Jeong, "Lissajous Scanning Two-photon Endomicroscope for In vivo Tissue Imaging," *Scientific Reports*, vol. 9, no. 1, p. 3560, Mar. 2019, number: 1 Publisher: Nature Publishing Group. [Online]. Available: <https://www.nature.com/articles/s41598-019-38762-w>
- [31] Y. Zhang, M. L. Akins, K. Murari, J. Xi, M.-J. Li, K. Luby-Phelps, M. Mahendroo, and X. Li, "A compact fiber-optic SHG scanning endomicroscope and its application to visualize cervical remodeling during pregnancy," *Proceedings of the National Academy of Sciences*, vol. 109, no. 32, pp. 12 878–12 883, Aug. 2012, publisher: Proceedings of the National Academy of Sciences. [Online]. Available: <https://www.pnas.org/doi/abs/10.1073/pnas.1121495109>
- [32] Y. Zhao, H. Nakamura, and R. J. Gordon, "Development of a versatile two-photon endoscope for biological imaging," *Biomedical Optics Express*, vol. 1, no. 4, pp. 1159–1172, Nov. 2010, publisher: Optica Publishing Group. [Online]. Available: <https://opg.optica.org/boe/abstract.cfm?uri=boe-1-4-1159>
- [33] F. Akhoundi, Y. Qin, N. Peyghambarian, J. K. Barton, and K. Kieu, "Compact fiber-based multi-photon endoscope working at 1700 nm," *Biomedical Optics Express*, vol. 9, no. 5, pp. 2326–2335, May 2018, publisher: Optica Publishing Group. [Online]. Available: <https://opg.optica.org/boe/abstract.cfm?uri=boe-9-5-2326>
- [34] L. Fu, A. Jain, H. Xie, C. Cranfield, and M. Gu, "Nonlinear optical endoscopy based on a double-clad photonic crystal fiber and a MEMS mirror," *Optics Express*, vol. 14, no. 3, pp. 1027–1032, Feb. 2006, publisher: Optica Publishing Group. [Online]. Available: <https://opg.optica.org/oe/abstract.cfm?uri=oe-14-3-1027>
- [35] Y.-C. Chang, J. Y. Ye, T. Thomas, Y. Chen, J. R. Baker, and T. B. Norris, "Two-photon fluorescence correlation spectroscopy through a dual-clad optical fiber," *Optics Express*, vol. 16, no. 17, pp. 12 640–12 649, Aug. 2008, publisher: Optica Publishing Group. [Online]. Available: <https://opg.optica.org/oe/abstract.cfm?uri=oe-16-17-12640>
- [36] D. R. Rivera, C. M. Brown, D. G. Ouzounov, I. Pavlova, D. Kobat, W. W. Webb, and C. Xu, "Compact and flexible raster scanning multiphoton endoscope capable of imaging unstained tissue," *Proceedings of the National Academy of Sciences*, vol. 108, no. 43, pp. 17 598–17 603, Oct. 2011, publisher: Proceedings of the National Academy of Sciences. [Online]. Available: <https://www.pnas.org/doi/full/10.1073/pnas.1114746108>
- [37] A. Li, H. Guan, H.-C. Park, Y. Yue, D. Chen, W. Liang, M.-J. Li, H. Lu, and X. Li, "Twist-free ultralight two-photon fiberscope enabling neuroimaging on freely rotating/walking mice," *Optica*, vol. 8, no. 6, pp. 870–879, Jun. 2021, publisher: Optica Publishing Group. [Online]. Available: <https://opg.optica.org/optica/abstract.cfm?uri=optica-8-6-870>
- [38] V. Kučikas, M. P. Werner, T. Schmitz-Rode, F. Louradour, and M. A. M. J. van Zandvoort, "Two-Photon Endoscopy: State of the Art and Perspectives," *Molecular Imaging and Biology*, vol. 25, no. 1, pp. 3–17, Feb. 2023. [Online]. Available: <https://doi.org/10.1007/s11307-021-01665-2>
- [39] A. Klioutchnikov, D. J. Wallace, M. H. Frosz, R. Zeltner, J. Sawinski, V. Pawlak, K.-M. Voit, P. S. J. Russell, and J. N. D. Kerr, "Three-photon head-mounted microscope for imaging deep cortical layers in freely

- moving rats,” *Nature Methods*, vol. 17, no. 5, pp. 509–513, May 2020, number: 5 Publisher: Nature Publishing Group. [Online]. Available: <https://www.nature.com/articles/s41592-020-0817-9>
- [40] D. M. Huland, K. Charan, D. G. Ouzounov, J. S. Jones, N. Nishimura, and C. Xu, “Three-photon excited fluorescence imaging of unstained tissue using a GRIN lens endoscope,” *Biomedical Optics Express*, vol. 4, no. 5, pp. 652–658, May 2013, publisher: Optica Publishing Group. [Online]. Available: <https://opg.optica.org/boe/abstract.cfm?uri=boe-4-5-652>
- [41] A. N. Kolyadin, G. K. Alagashev, A. D. Pryamikov, L. Mouradian, A. Zeytunyan, H. Toneyan, A. F. Kosolapov, and I. A. Bufetov, “Negative Curvature Hollow-core Fibers: Dispersion Properties and Femtosecond Pulse Delivery,” *Physics Procedia*, vol. 73, pp. 59–66, Jan. 2015. [Online]. Available: <https://www.sciencedirect.com/science/article/pii/S1875389215012924>
- [42] C. Wei, R. J. Weiblen, C. R. Menyuk, and J. Hu, “Negative curvature fibers,” *Advances in Optics and Photonics*, vol. 9, no. 3, pp. 504–561, Sep. 2017, publisher: Optica Publishing Group. [Online]. Available: <https://opg.optica.org/aop/abstract.cfm?uri=aop-9-3-504>
- [43] B. Debord, A. Amsanpally, M. Chafer, A. Baz, M. Maurel, J. M. Blondy, E. Hugonnot, F. Scol, L. Vincetti, F. Gérôme, and F. Benabid, “Ultralow transmission loss in inhibited-coupling guiding hollow fibers,” *Optica*, vol. 4, no. 2, pp. 209–217, Feb. 2017, publisher: Optica Publishing Group. [Online]. Available: <https://opg.optica.org/optica/abstract.cfm?uri=optica-4-2-209>
- [44] M. Tateda, N. Shibata, and S. Seikai, “Interferometric method for chromatic dispersion measurement in a single-mode optical fiber,” *IEEE Journal of Quantum Electronics*, vol. 17, no. 3, pp. 404–407, Mar. 1981, conference Name: IEEE Journal of Quantum Electronics. [Online]. Available: <https://ieeexplore.ieee.org/abstract/document/1071115>
- [45] M. Zeisberger and M. A. Schmidt, “Analytic model for the complex effective index of the leaky modes of tube-type anti-resonant hollow core fibers,” *Scientific Reports*, vol. 7, no. 1, p. 11761, Sep. 2017, number: 1 Publisher: Nature Publishing Group. [Online]. Available: <https://www.nature.com/articles/s41598-017-12234-5>
- [46] K. Iga, “Theory for gradient-index imaging,” *Applied Optics*, vol. 19, no. 7, pp. 1039–1043, Apr. 1980, publisher: Optica Publishing Group. [Online]. Available: <https://opg.optica.org/ao/abstract.cfm?uri=ao-19-7-1039>
- [47] J. P. Thirion, “Image matching as a diffusion process: an analogy with Maxwell’s demons,” *Medical Image Analysis*, vol. 2, no. 3, pp. 243–260, Sep. 1998. [Online]. Available: <https://www.sciencedirect.com/science/article/pii/S1361841598800224>
- [48] P. Mahou, G. Malkinson, E. Chaudan, T. Gacoin, E. Beaufrepaire, and W. Supatto, “Metrology of Multiphoton Microscopes Using Second Harmonic Generation Nanoprobes,” *Small*, vol. 13, no. 42, p. 1701442, 2017, eprint: <https://onlinelibrary.wiley.com/doi/pdf/10.1002/sml.201701442>. [Online]. Available: <https://onlinelibrary.wiley.com/doi/abs/10.1002/sml.201701442>
- [49] W. R. Zipfel, R. M. Williams, and W. W. Webb, “Nonlinear magic: multiphoton microscopy in the biosciences,” *Nature Biotechnology*, vol. 21, no. 11, pp. 1369–1377, Nov. 2003, publisher: Nature Publishing Group. [Online]. Available: <https://www.nature.com/articles/nbt899>
- [50] H.-C. Park, H. Guan, A. Li, Y. Yue, M.-J. Li, H. Lu, and X. Li, “High-speed fiber-optic scanning nonlinear endomicroscopy for imaging neuron dynamics in vivo,” *Optics Letters*, vol. 45, no. 13, pp. 3605–3608, Jul. 2020, publisher: Optica Publishing Group. [Online]. Available: <https://opg.optica.org/ol/abstract.cfm?uri=ol-45-13-3605>
- [51] Y. Wu, Y. Zhang, J. Xi, M.-J. Li, and X. Li, “Fiber-optic nonlinear endomicroscopy with focus scanning by using shape memory alloy actuation,” *Journal of Biomedical Optics*, vol. 15, no. 6, p. 060506, Nov. 2010, publisher: SPIE. [Online]. Available: <https://www.spiedigitallibrary.org/journals/journal-of-biomedical-optics/volume-15/issue-6/060506/Fiber-optic-nonlinear-endomicroscopy-with-focus-scanning-by-using-shape/10.1117/1.3523234.full>
- [52] A. Li, W. Liang, H. Guan, Y.-T. A. Gau, D. E. Bergles, and X. Li, “Focus scanning with feedback-control for fiber-optic nonlinear endomicroscopy,” *Biomedical Optics Express*, vol. 8, no. 5, pp. 2519–2527, May 2017, publisher: Optica Publishing Group. [Online]. Available: <https://opg.optica.org/boe/abstract.cfm?uri=boe-8-5-2519>
- [53] A. Lombardini, E. R. Andresen, A. Kudlinski, I. Rimke, and H. Rigneault, “Origin and suppression of parasitic signals in Kagomé lattice hollow core fibers used for SRS microscopy and endoscopy,” *Optics Letters*, vol. 42, no. 9, pp. 1824–1827,
- May 2017, publisher: Optica Publishing Group. [Online]. Available: <https://opg.optica.org/ol/abstract.cfm?uri=ol-42-9-1824>

## APPENDIX C BIOGRAPHY SECTION

### Authors:



**Dylan Septier** studied experimental physics before earning a Ph.D. in optics from the University of Lille, focusing on double clad hollow core fibers for nonlinear endoscopy. Dr Septier currently serves as an R&D engineer at Lightcore Technologies, specializing in developing advanced optical technologies.



**Gaëlle Brévalle-Wasilewski** graduated in Materials Science from PolytechLille in 2016 and obtained her Ph.D. degree in photonics from INSA Rennes in the field of QDs dual-frequency VECSELS in 2019. After a post-doctoral position at the PhLAM laboratory, she joined Lightcore Technologies in 2021 to develop the nonlinear endoscope and its applications.



**Eloise Lefebvre** graduated in physical engineering, is currently pursuing her doctoral studies within the PhLAM laboratory in collaboration with Lightcore Technologies. Her research project focuses on the development of a miniaturized endoscope specifically dedicated to real-time Raman histopathology.



**Naveen Gajendra Kumar** completed his masters in Optics and Photonics at Aix Marseille University and Karlsruhe Institute of Technology under the Erasmus Mundus Europhotonics program in 2019 after which he started his PhD on the subject of Endoscopy for in-vivo TPEF imaging of neurons in mice under at Institut Fresnel. In March 2023 he successfully defended his PhD thesis. He joined Lightcore technologies in 2023 to develop fluorescence and nonlinear microscopes and endoscope.



**Yong Jian Wang** is a research engineer at Lightcore Technologies in Marseille, France. Dr. Wang has spent more than ten years in biophysical research after receiving his Ph.D. in Physics at Hong Kong University of Science and Technology. At Lightcore Technologies, he is responsible for developing the multimodal microscope and endoscope for use in both fundamental scientific research and biomedical applications.



**Attila Kaszas** received his MSc degree in Biology from Eötvös Loránd University in Budapest in 2006, and his PhD degree in Neuroscience from Semmelweis University in 2012. He has been involved in combining novel imaging methods and neurotechnology in studying various neurological conditions such as epilepsy, the development of glioblastomas and Parkinson's disease. He is affiliated to HUN-REN Research Centre for Natural Sciences. He joined Lightcore Technologies in 2024 as an application scientist in neurosciences.



**Hervé Rigneault** received his Engineering degree from the Ecole Nationale Supérieure de Physique de Marseille in 1991, and his Ph.D. degrees in optical engineering from Aix-Marseille Univ in 1993. He joined the Centre National de la Recherche Scientifique in 1994 where he is a CNRS Research Director at the Institut Fresnel. He has authored more than 230 peer-reviewed journal papers and is a co-inventor of 17 patents in the field of optical engineering and molecular spectroscopy.



**Alexandre Kudlinski** received his PhD degree in Optics from University of Lille in 2005. He was a research officer at University of Bath from 2005 to 2006. In 2006, he joined University of Lille as a lecturer where he was appointed Professor in 2016. He has co-authored more than 160 papers in nonlinear photonics and micro-endoscopy and holds 7 patents.